Front. Phys. 12(3), 127209 (2017)
DOI 10.1007/s11467-017-0663-0

RESEARCH ARTICLE

Two-carrier transport in $SrMnBi_2$ thin films

Xiao Yan[1], Cheng Zhang[2,3], Shan-Shan Liu[2,3], Yan-Wen Liu[2,3], David Wei Zhang[1], Fa-Xian Xiu[2,3,†], Peng Zhou[1,‡]

[1] *State Key Laboratory of ASIC and System, School of Microelectronics, Fudan University, Shanghai 200433, China*
[2] *State Key Laboratory of Surface Physics and Department of Physics, Fudan University, Shanghai 200433, China*
[3] *Collaborative Innovation Center of Advanced Microstructures, Nanjing 210093, China*
Corresponding authors. E-mail: †faxian@fudan.edu.cn, ‡pengzhou@fudan.edu.cn
Received January 11, 2017; accepted February 27, 2017

Monocrystalline $SrMnBi_2$ thin films were grown by molecular beam epitaxy (MBE), and their transport properties were investigated. A high and unsaturated linear magnetoresistance (MR) was observed, which exhibited a transition from a semi-classical weak-field B^2 dependence to a high-field linear dependence. An unusual nonlinear Hall resistance was also observed because of the anisotropic Dirac fermions. The two-carrier model was adopted to analyze the unusual Hall resistance quantitatively. The fitting results yielded carrier densities and mobilities of 3.75×10^{14} cm^{-2} and 850 $cm^2 \cdot V^{-1} \cdot s^{-1}$, respectively, for holes, and 1.468×10^{13} cm^{-2}, 4118 $cm^2 \cdot V^{-1} \cdot s^{-1}$, respectively, for electrons, with a hole-dominant conduction at 2.5 K. Hence, an effective mobility can be achieved, which is in reasonable agreement with the effective hole mobility of 1800 $cm^2 \cdot V^{-1} \cdot s^{-1}$, extracted from the MR. Further, the angle-dependent MR, proportional to cos θ, where θ is the angle between the external magnetic field and the perpendicular orientation of the sample plane, also implies a high anisotropy of the Fermi surface. Our results about $SrMnBi_2$ thin films, as one of a new class of $AEMnBi_2$ and $AEMnSb_2$ (AE = Ca, Sr, Ba, Yb, Eu) materials, suggest that they have a lot of exotic transport properties to be investigated, and that their high mobility might facilitate electronic device applications.

Keywords $SrMnBi_2$, thin films, magnetoresistance, two carriers, anisotropic Dirac fermions

PACS numbers 68.90.+g, 74.78.-w, 81.15.Hi

1 Introduction

Dirac materials, such as graphene [1, 2] and topological insulators (TIs) [3, 4], have attracted great attention, owing to their unique properties, such as high carrier mobility with forcefully-suppressed backscattering [5], anomalous half-integer quantum Hall effect carrying the nonzero Berry phase [6, 7], and a large linear and unsaturated magnetoresistance (MR) [5, 8, 9], resulting from the linear energy dispersion around the Dirac points Therefore, graphene and many other Dirac materials have been applied to multifarious electronic devices [10, 11]. In particular, graphene is expected to substitute silicon in integrated circuits [11, 12].

$AEMnBi_2$ and $AEMnSb_2$ (AE = Ca, Sr, Ba, Yb, Eu) constitute a new class of Dirac materials [13–17]. Taking $SrMnBi_2$ as an example, the crystal structure of $SrMnBi_2$ belongs to the space group I4/mmm, and is comprised of a layer of MnBi consisting of edge-sharing tetrahedra and a Bi square net, separated by an electronegative Sr layer [18, 19], as shown in Fig. 1(a). Most electronic states near the Fermi level originate from the Bi square net instead of the MnBi layer, because there are energy levels separating the electronic states in the MnBi layer from the Fermi level [20]. Thus, the Bi square net is responsible for the linear energy-momentum dispersion as seen in graphene. Recently, a highly anisotropic Dirac cone in $SrMnBi_2$ was theoretically predicted and experimentally observed [19]. The Dirac cones in graphene and topological insulators are usually isotropic, unless external periodic potentials [14, 19] and mechanical stress are applied [21]. $SrMnBi_2$, containing a Bi square net, provides a new route for controlling the anisotropy of the Dirac cone. Recently, the transport properties of bulk $SrMnBi_2$ single crystals have been investigated, and the unsaturated MR resulting from the linear energy dispersion,

*Special Topic: Recent Progress on Weyl Semimetals (Eds. Xincheng Xie, Xian-Gang Wan, Hong-Ming Weng & Hua Jiang).

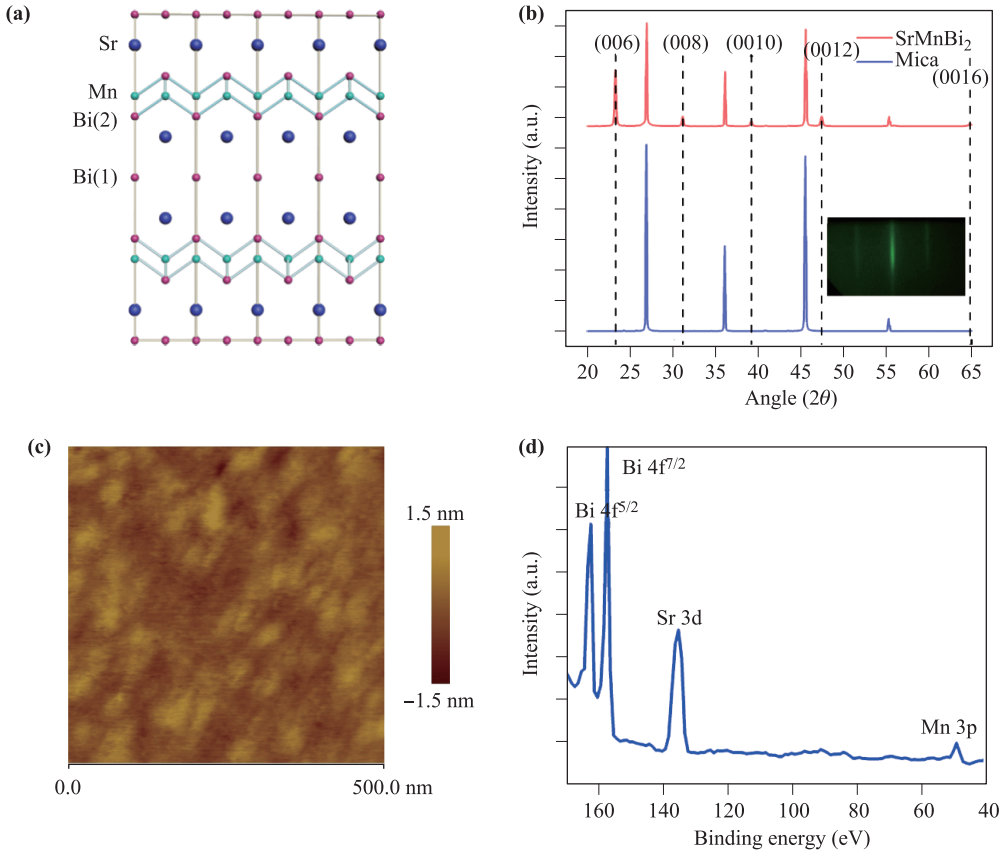

Fig. 1 **(a)** Crystal structure of $SrMnBi_2$. The inset shows the *in-situ* RHEED patterns of the thin films. **(b)** XRD pattern and **(c)** Surface morphology of the $SrMnBi_2$ thin films on mica, probed by atomic force microscopy. The RMS is 0.3 nm with a scan size of 500 nm. **(d)** X-ray photoemission spectrum of $SrMnBi_2$ thin films. The characteristic peaks of Sr 3d, Mn 3p, Bi $4f^{5/2}$, and $4f^{7/2}$ are marked in the spectrum.

angular dependent MR, and oscillations have been observed, illustrating the dominant two-dimensional (2D) Dirac fermion states in $SrMnBi_2$ [19]. However, there is limited work on $SrMnBi_2$ thin films, which are expected to exhibit new properties originating from the dimensional change.

Here, we report the growth of $SrMnBi_2$ monocrystalline thin films with a molecular beam epitaxy (MBE) system and its transport properties. The unsaturated MR was observed and it exhibited a crossover at a critical B^* from a semi-classical low-field B^2 dependence to a high-field linear dependence. The nonlinear transverse resistance (R_{xy}) validates the two-carrier conduction in $SrMnBi_2$, which is in accordance its multiband, Dirac, and conventional parabolic band states [22, 23].

2 Growth and characterization

Monocrystalline thin films of $SrMnBi_2$ were grown in a Perkin-Elmer MBE. The basic pressure reached 1×10^{-9} mbar. The mica substrates were freshly cleaved and preheated to 400 °C for 30 min. The source cells of Sr (99.999%), Mn (99.999%), and Bi (99.999%) were heated up to ensure a beam-flux ratio of approximately 2:1:20, which was measured *in-situ* by FTM-2400 quartz monitor crystal. The crystal structure and quality of $SrMnBi_2$ thin films were examined by X-Ray diffraction (XRD) with Cu-Kα radiation, as shown in Fig. 1(b). The XRD pattern shows the (00l) reflections, which match those in previous reports [18]. The high crystallinity can be verified by the small full-width-at-half-maximum (FWHM) of the (006) plane, which is 0.288°, as well as the reflection high-energy electronic diffraction (RHEED) streak patterns [Fig. 1(b) inset]. Figure 1(c) displays the surface topography of $SrMnBi_2$ on mica with a root mean square (RMS) of approximately 0.3 nm. The X-ray photoemission spectroscopy (XPS) of $SrMnBi_2$ thin films is shown in Fig. 1(d), where the peaks of Sr 3d, Mn 3p, and Bi $4f^{5/2}$ and $4f^{7/2}$ (spin-orbit split doublet) core levels are evident. There are no other extra peaks, implying a good surface quality.

3 Results and discussion

3.1 Temperature-dependent longitudinal resistance

The transport properties were analyzed in a Quantum Design Physical Property Measurement System (PPMS-9) with a standard six-probe Hall Bar [Fig. 2(a)]. The longitudinal resistance (R_{xx}) was acquired by measuring the voltage drop between electrodes 2 and 3 or between electrodes 6 and 5, when applying a constant current source to electrodes 1 and 4. The value of R_{xx} decreases along with the decline in the temperature, illustrating a metallic behavior, as shown in Fig. 2(b). When the temperature is reduced below 5 K, R_{xx} has a tendency to decrease slowly and even slightly increase, similar to the traditional case of a metal with magnetic impurities, as seen in the Kondo effect [24], which can be described as

$$\rho(T) = \rho_0 + aT^2 + c_m \ln\frac{\mu}{T} + bT^5, \quad (1)$$

where ρ_0 is the residual resistance and a, c_m, and b are constants, derived from the Fermi liquid properties, the lattice vibrations, and the logarithmic dependence, respectively. By fitting the R_{xx}–T curves at low temperature with Eq. (1) in the inset of Fig. 2(b), ρ_0, a, c_m, and b can be obtained; their values being 2.345 Ω, 5.6×10^{-4} Ω·T^{-2}, 0.025, and 6.58×10^{-9} T^{-5}, respectively. The resistivity of our $SrMnBi_2$ thin films is lower than that of the bulk $SrMnBi_2$ single crystals [18].

The thickness of the thin films is approximately 300 nm. The temperature-dependent behavior of R_{xx} unambiguously depends on the thickness, as provided in the Appendix, Fig. A1. All thin films with different thicknesses have a metallic behavior, similar to that shown in Fig. 2(b). The large, positive, and unsaturated MR (MR = $[R_{xx}(B) - R_{xx}(0)]/R_{xx}(0)$) at different temperatures is illustrated in Fig. 2(c). It is linearly dependent on the external magnetic field up to 9 T, while it has a semi-classical quadratic dependence when it comes to a low field range. The MR increases by 116.5% at 2.5 K and 9 T. A linear unsaturated MR is widely observed in Dirac materials. The MR can be fitted with MR = A_2B^2 in the low-field region ($B < 1$ T) and MR = $A_1B+O(B^2)$ in the high-field region, which can be acquired directly by the derivative of MR [d(MR)/dB] as shown in Fig. 2(d).

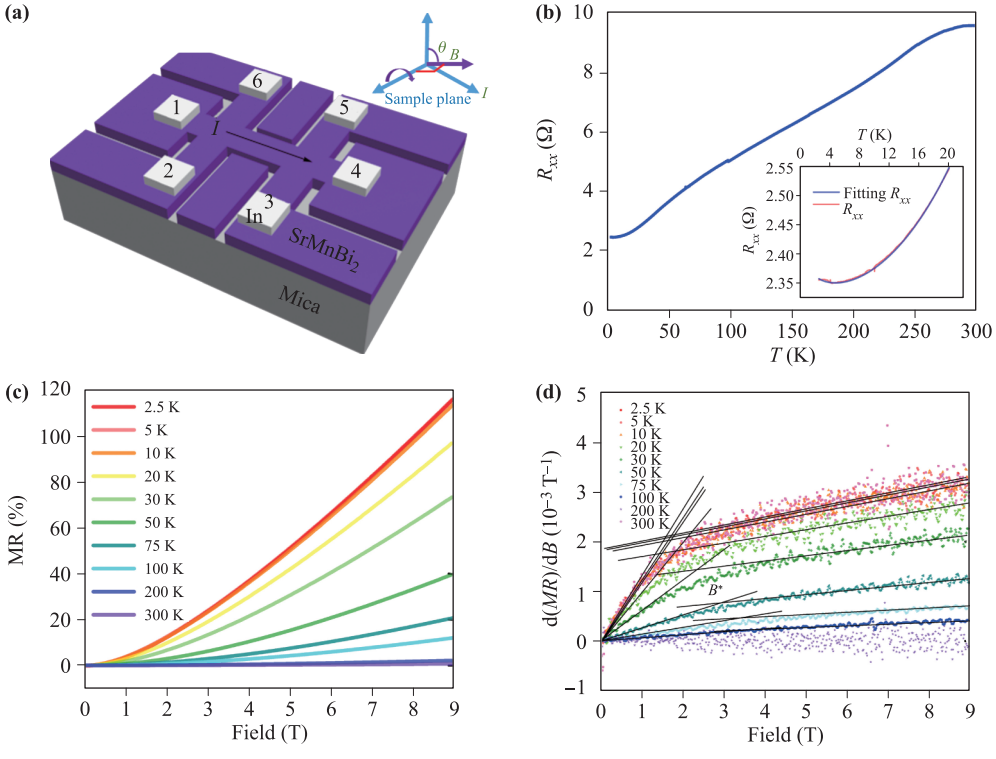

Fig. 2 **(a)** Schematic diagram of the transport measurement with the conventional four-wire method, using a standard six-probe Hall bar. The inset shows the direction of the field relative to the sample plane and the direction of current. **(b)** Temperature (T) dependence of R_{xx} at $B = 0$ T with a metallic behavior, in accordance with the Kondo Effect at low temperatures (inset). **(c)** Magnetoresistance (MR) changes at different temperatures. **(d)** The derivative of the MR with respect to the magnetic field at different temperatures. The coefficients of A_1 and critical B^* versus T by fitting the MR in the high-field regions with MR = $A_1B+O(B^2)$, and in the low-field regions with MR = A_2B^2, which intersect at the critical B^*.

The fitting lines in the low-field and high-field regions intersect with each other at the critical filed B^*, which is considered to be the crossing point between the semiclassical and the quantum linear transport regimes. The large unsaturated MR is comparable to that observed in bulk $SrMnBi_2$, and a transition between the semiclassical weak-field B square dependence and a high-field linear dependence was also found in $SrMnBi_2$ [18].

3.2 Two-carrier model fitting

Although the large linear MR provides direct evidence of the Dirac cone states, there should be both Dirac carriers and parabolic-band carriers involved in the conduction in the multiband system. The anisotropic Dirac fermions have been observed directly by angle-resolved photoelectron spectroscopy (ARPES) [19]. The Hall resistance (R_{xy}), as shown in Fig. 3(a), is acquired by measuring the voltage between electrodes 2 and 6 or between electrodes 3 and 5 when applying a constant current source between electrodes 1 and 4, with a magnetic field (up to 9 T) perpendicular to the plane. The nonlinear Hall conduction can be easily observed at low temperatures, suggesting an evident two-carrier transport, while it is approximately linear when the temperature is above 100 K. The slope of the Hall resistance is positive, signaling the dominance of holes instead of electrons in the conduction. However, the slope of R_{xy} is negative in the low field region in the thin films, shown in the Appendix, Fig. A5, which suggests the dominance of electrons in the conduction. In the high-field limit, R_{xy} is proportional to $\frac{1}{e(n_h-n_e)}$, where n_h and n_e are the carrier densities of holes and electrons, respectively. In addition, the presence of the two types of carriers with different scattering times (τ), can be validated by a scaling relation — Kohler's rule given by

$$\frac{\Delta R_{xx}(B,T)}{R_{xx}(0,T)} = f\left(\frac{B}{R_{xx}(0,T)}\right), \tag{2}$$

which can be applied to the system with a constant τ over the Fermi surfaces [25, 26]. Figure 3(b) illustrates the Kohler plots at different temperatures. The temperature-dependent Kohler plots at different temperatures do not overlap with each other, while they should overlap with each other if there is only one type of carrier. The unusual nonlinear Hall resistance have not observed

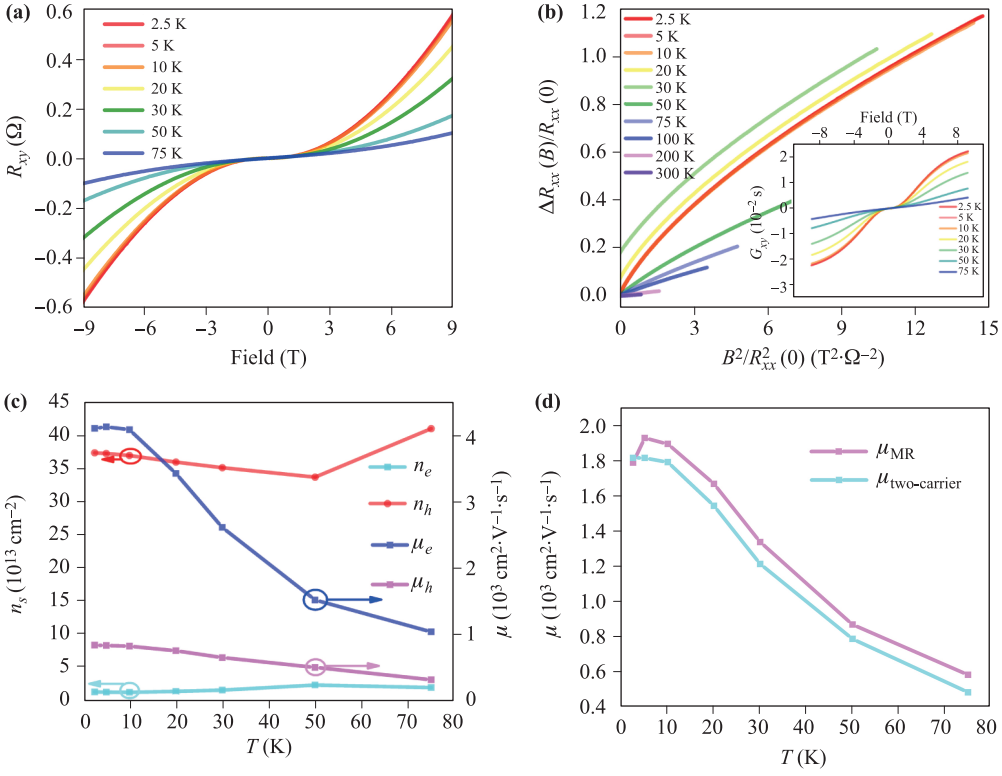

Fig. 3 **(a)** R_{xy} at different temperatures. **(b)** Kohler plots of the MR curves. The inset shows the Hall conductance $[G_{xy} = R_{xy}/(R_{xx}^2 + R_{xy}^2)]$ at different temperatures, fitted by the two-carrier model. **(c)** Fitting results with mobility and sheet carrier density of holes and electrons after the two-carrier model fitting. **(d)** The inset is the temperature-dependent effective MR mobility $[\mu_{MR} = \frac{\sqrt{\sigma_e\sigma_h}}{\sigma_e+\sigma_h}(\mu_e + \mu_h) = \sqrt{A_2}]$ extracted from the low-field MR (*pink line*) compared with that calculated by the two-carrier model (*blue line*).

in bulk $SrMnBi_2$, but clear Shubnikov–de Haas (sdH) oscillations were observed, which are a strong evidence for the existence of Dirac fermions in $SrMnBi_2$ [20]. it is highly likely that the unusual nonlinear Hall resistance to derives from dimensionality reduction.

We employed the two-carrier model to analyze the transport properties of our thin films with the following equation [25, 27]:

$$R_{xy} = \frac{n_h\mu_h^2 - n_e\mu_e^2 + (\mu_e\mu_h B)^2(n_h - n_e)}{e[(n_h\mu_h + n_e\mu_e)^2(\mu_e\mu_h B)^2(n_h - n_e)^2]}, \quad (3)$$

where μ_h and μ_e are the mobilities of holes and electrons, respectively. As the Hall resistance is low, we adopted the Hall conductance $G_{xy} = \frac{R_{xy}}{R_{xy}^2+R_{xx}^2}$ [the inset of Fig. 3(b)] for the fitting model to improve the accuracy of the fitting results. It obeys the corresponding equation:

$$G_{xy} = e\left(\frac{n_e\mu_e^2 B}{\mu_e^2 B^2 + 1} + \frac{n_h\mu_h^2 B}{\mu_h^2 B^2 + 1}\right). \quad (4)$$

With the best fit to Eq. (4), the temperature-dependent mobility and sheet carrier density of holes and electrons can be obtained, as shown in Fig. 3(c). The mobility of both holes and electrons increases with the decrease in temperature, due to the decline of the scattering in the crystal structure and the density of carriers However, the sheet density of holes decreases while that of electrons increases, as the temperature decreases. The mobility of holes increases from 500 $cm^2{\cdot}V^{-1}{\cdot}s^{-1}$ to 850 $cm^2{\cdot}V^{-1}{\cdot}s^{-1}$, and that of electrons increases from 1530 $cm^2{\cdot}V^{-1}{\cdot}s^{-1}$ to 4000 $cm^2{\cdot}V^{-1}{\cdot}s^{-1}$, when the temperature decreases from 50 to 2.5 K. However, the sheet density of holes increases from 3.4×10^{14} cm^{-2} to 3.7×10^{14} cm^{-2} while that of electrons declines from 2.5×10^{13} cm^{-2} to 1.5×10^{13} cm^{-2}, which verifies our qualitative analysis of the domination of holes in the conduction, as previously mentioned.

In the multiband system, the MR in the semi-classical transport can be described as $\mathrm{MR} = \frac{\sigma_e\sigma_h(\mu_e+\mu_h)^2}{(\sigma_e+\sigma_h)^2}B^2$, where σ_e, σ_h, μ_e, and μ_h are all in the zero field, when the Dirac carriers dominate the transport [18]. Therefore, the effective MR mobility, $\mu_{\mathrm{MR}} = \frac{\sqrt{\sigma_e\sigma_h}}{\sigma_e+\sigma_h}(\mu_e+\mu_h)$, is equal to the coefficient of the low-field B^2 quadratic term $\sqrt{A_2}$, as shown in the inset of Fig. 3(d) with the blue line. In effect, $\mu_{\mathrm{MR}} \leqslant \frac{1}{2}(\mu_e+\mu_h) = \mu_{ave}$, which gives the lower bound of the average mobility of holes and electrons [22], which is in accordance with the fitting result of the two-carrier model described above. Since the conductivities of the electrons and holes are given by $\sigma_e = n_e\mu_e e$ and $\sigma_h = n_h\mu_h e$, respectively, the effective μ can be acquired by the fitting results of the two-carrier model, as shown in Fig. 3(d) with the blue line, with $\mu_{two\text{-}carrier} = \frac{\sqrt{n_e\mu_e n_h\mu_h}}{n_e\mu_e+n_h\mu_h}(\mu_e+\mu_h)$. The mobilities acquired with the MR fitting and two-carrier model practically overlap with each other, verifying the accuracy of our fitting results. μ_{MR} and the coefficient of the high-field linear term A_1 decrease as the temperature declines, because the thermal fluctuation smears the Landau level splitting [18]. The effective mobility of $SrMnBi_2$ thin films is lower than that of the $SrMnBi_2$ bulk (3400 $cm^2{\cdot}V^{-1}{\cdot}s^{-1}$) [18]. The MR and R_{xy} of thin films with different thickness are shown in the Appendix, Figs. A2–A6.

3.3 Angular-dependent MR and Hall resistance

The angle-dependent MR and Hall resistance at $T = 2.5$ K are illustrated in Figs. 4(a) and (b), respectively. The tilt angle θ refers to the angle between the directions of the current and the magnetic field while the sample plane is perpendicular to the plane containing the current and the field, through which the sample holder can be rotated, as shown in the inset of Fig. 2(a). MR and R_{xy} show a significant angular dependence. When B is perpendicular to the sample plane, the largest MR and R_{xy} can be obtained, and as θ increases, MR and R_{xy} gradually decrease. When the current is parallel to B, R_{xy} is negligible while MR is not zero, which

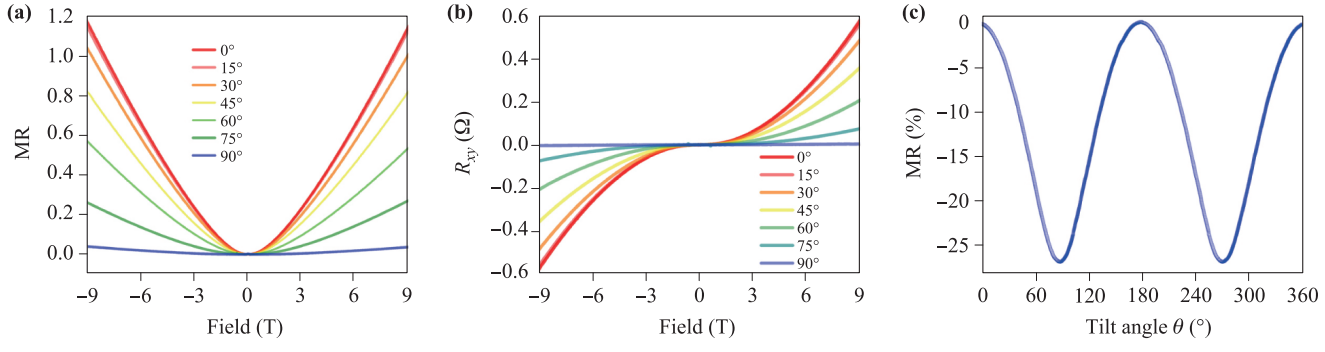

Fig. 4 **(a)** MR and **(b)** R_{xy} vs. the external magnetic field B, with different tilt angles (θ) at 2.5 K. **(c)** MR versus the tilt angle θ (from 0° to 360°) at $B = 9$ T.

is due to the carrier scattering. The variation of MR along with the rotation of the sample plane (tilt angle θ) follows the relationship MR $= a + b\cos\theta$ with a period of 180°, as shown in Fig. 4(c) (This sample has a thickness of approximately 80 nm). Therefore, the transfer integral and the coupling between layers along the c axis in the Brillouin zone should be small and the Fermi surface should be anisotropic with much lower carrier mobility along the k_z plane, and higher carrier mobility along the k_x and k_y planes. The anisotropy of thin films with different thickness is provided in the Appendix, Fig. A7.

4 Summary

In conclusion, we investigated the transport properties of a Dirac semimetal thin film of $SrMnBi_2$. We grew single-crystal thin films of $SrMnBi_2$ with good quality, and observed a large unsaturated linear MR similar to that in bulk $SrMnBi_2$. Further, the MR experiences a transition at a critical B^*, from a semi-classical weak-field B^2 dependence to a high-field linear dependence. An unusual nonlinear Hall resistance was observed because of the anisotropic Dirac fermions. We adopted the two-carrier model to quantitatively analyze the unusual Hall resistance, and the fitting results demonstrated the carrier density and mobility of holes and electrons, in good agreement with the effective MR mobility of 1800 $cm^2 \cdot V^{-1} \cdot s^{-1}$ at 2.5 K. Moreover, the angle-dependent MR, proportional to $\cos\theta$, implies a high anisotropy in the Fermi surface. Therefore, our findings in $SrMnBi_2$ thin films can be a platform for investigating other materials such as thin films of $AEMnBi_2$ and $AEMnSb_2$ (AE = Ca, Sr, Ba, Yb, Eu) classes.

Acknowledgements This work was supported in part by the National Key Research and Development Program (Grant No. 2016YFA0203900) and the National Natural Science Foundation of China (Grant Nos. 61376093, 61622401, 61322407, 11474058, and 61674040).

Appendix A Temperature dependence

Figure A1 illustrates the temperature dependence of R_{xx} in $SrMnBi_2$ thin films with different thickness, 50 nm, 80 nm, 100 nm, 170 nm, 300 nm, respectively, which was measured by the DektakXT Step Profiler. R_{xx} of all the thin films decline with the decrease of temperature; and the thicker of the thin films, the smaller of the resistances are, which follow Ohmic's law in general. No phase transition has been observed as the thickness decreases even down to 50 nm.

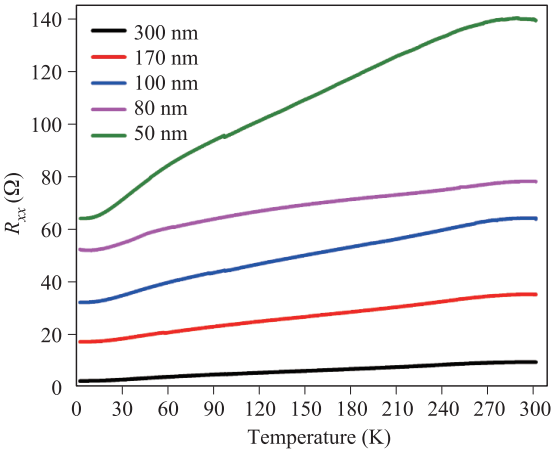

Fig. A1 Temperature dependence of R_{xx} in $SrMnBi_2$ thin films with different thickness. The thickness of these thin films ranges from ~50 nm to ~300 nm, and their resistance declines along with the decrease of temperature, exhibiting a metallic behavior.

Appendix B The longitudinal resistance (R_{xx}) vs. field (B)

All the transport properties in the main text come from the intrinsic nature of $SrMnBi_2$ thin films instead of a coincidence. Figure A2 demonstrates the transport properties of the samples with different thickness of (a) 170 nm, (b) 100 nm, (c) 80 nm, (d) 50 nm and the sample in the main text has a thickness of 300 nm.

MR exhibits a quadratic relationship to field B at low-field region and a unsaturated linear relationship at high-field region even up to ±9 T. It increases with the increase of B, and the largest MR is 40.3% (2.5 K), 36.7% (2.5 K), 38.0% (2.5 K), 36.6% (3 K) at $B = 9$ T for the four thin films with different thickness, respectively. The linear unsaturated magnetoresistance and the derivation from the traditional semi-classical transport in $SrMnBi_2$ are derived from the linear energy dispersion. We fitted MR with MR $= A_2B^2$ in low-field region ($B < 1$ T) and MR $= A_1B + O(B^2)$ in high-field region. In the two field region the two fitting lines intersect with each other at a critical field, B^* at each temperature.

Appendix C Hall resistance (R_{xy}) vs. field (B)

The presence of the two kinds of carriers with different scattering time, τ, can be validated by a scaling relation, Kohler's rule,

$$\frac{\Delta R_{xx}(B,T)}{R_{xx}(0,T)} = f\left(\frac{B}{R_{xx}(0,T)}\right),$$

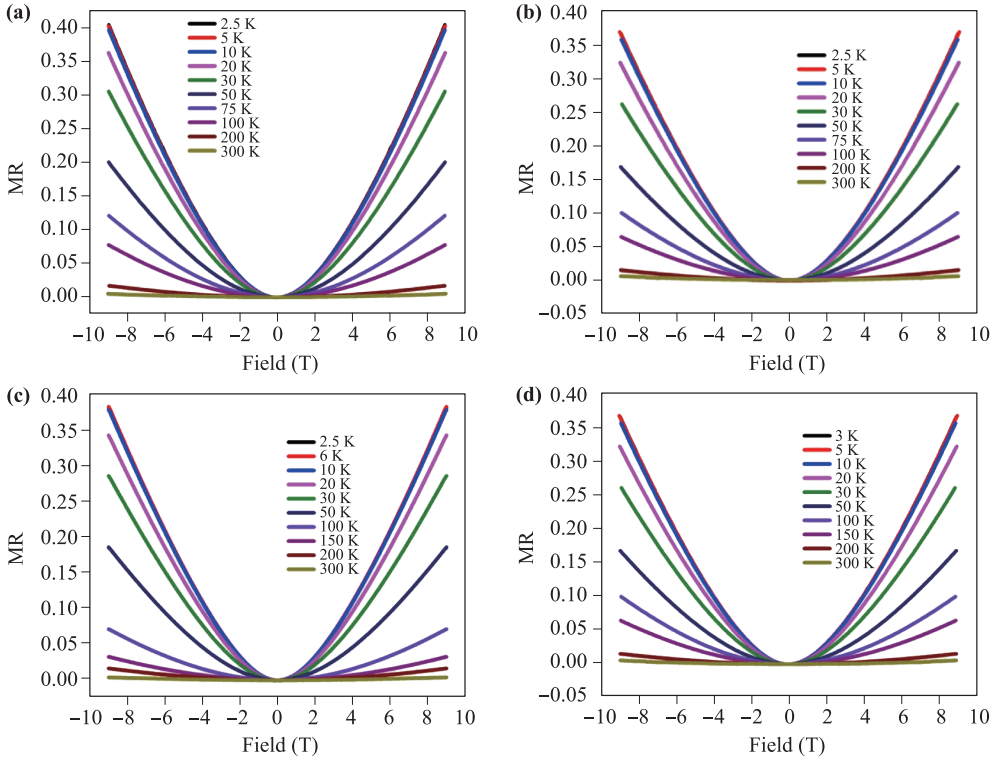

Fig. A2 Magnetic resistance MR = $\frac{R_{xx}(B)-R_{xx}(0)}{R_{xx}(0)}$ of thin films with different thickness of **(a)** 170 nm, **(b)** 100 nm, **(c)** 80 nm, **(d)** 50 nm. The lower the temperature is, the larger the MR will be.

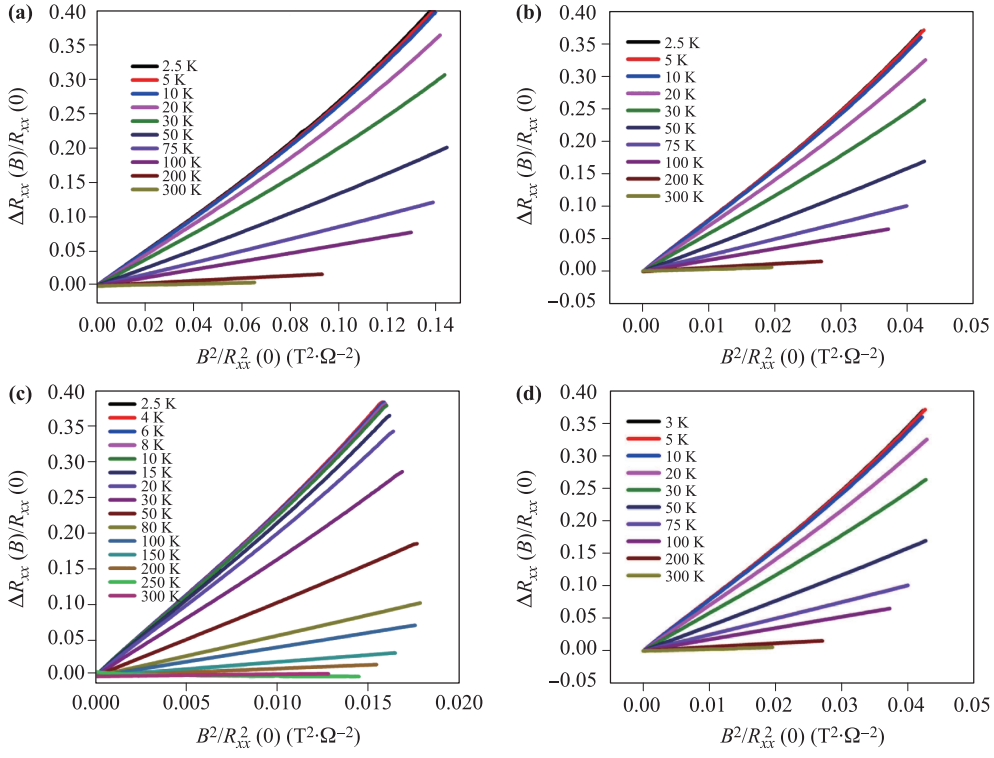

Fig. A3 The Kohler plots of the MR curves of thin films with different thickness of **(a)** 170 nm, **(b)** 100 nm, **(c)** 80 nm, **(d)** 50 nm. The Kohler plots do not overlap with each other, signaling that there are more than one kinds of carrier.

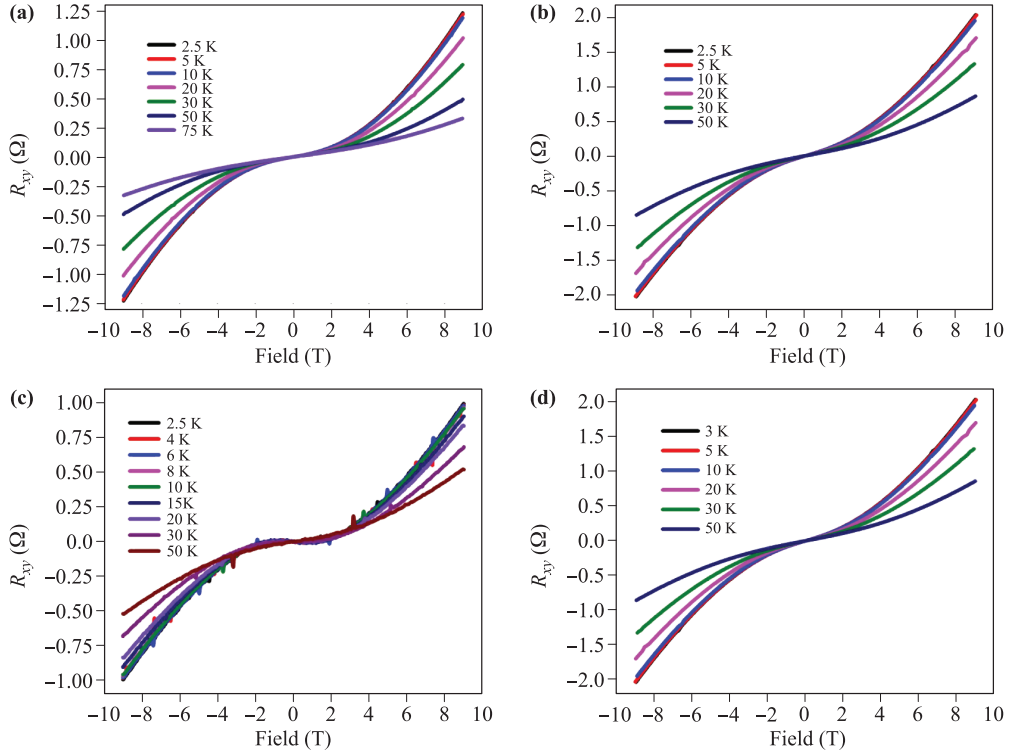

Fig. A4 Hall resistance (R_{xy}) vs. magnetic field (B) of thin films with different thickness of **(a)** 170 nm, **(b)** 100 nm, **(c)** 80 nm, **(d)** 50 nm at different temperatures.

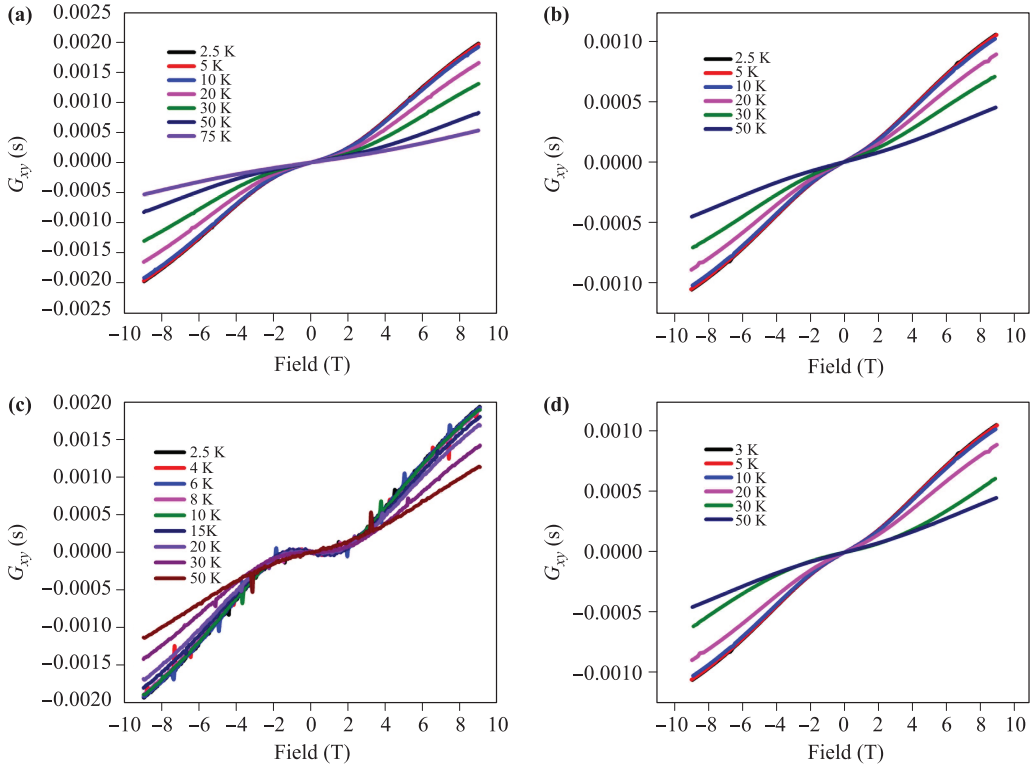

Fig. A5 Hall conductance [$G_{xy} = R_{xy}/(R_{xx}^2 + R_{xy}^2)$] of thin films with different thickness of **(a)** 170 nm, **(b)** 100 nm, **(c)** 80 nm, **(d)** 50 nm at different temperatures, and they are fitted by the two-carrier model.

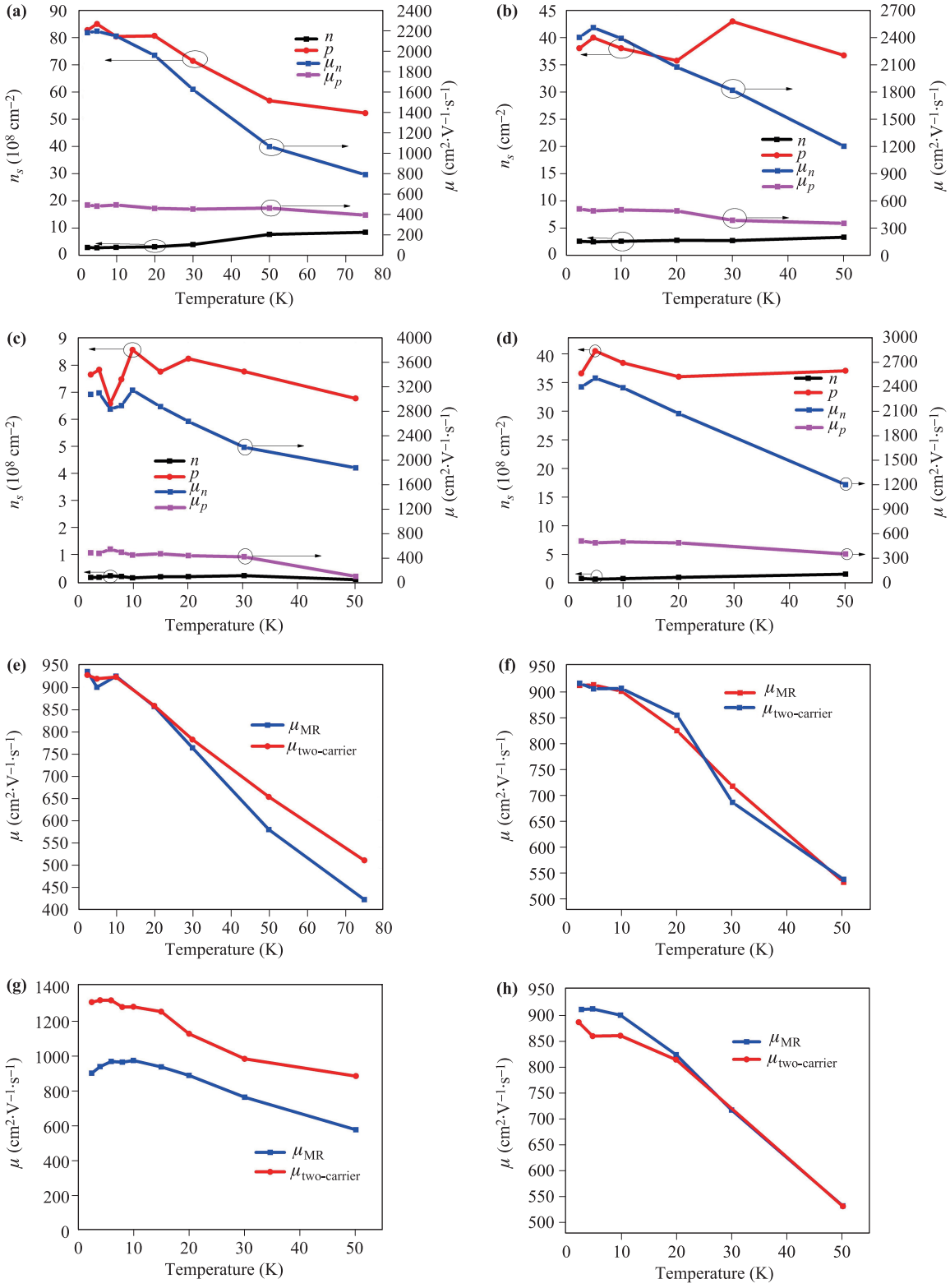

Fig. A6 Fitting parameters yielded by two-carrier model. Sheet density of thin films with different thickness of **(a)** 170 nm, **(b)** 100 nm, **(c)** 80 nm, **(d)** 50 nm at different temperatures and the temperature-dependent effective MR mobility $[\mu_{MR} = \frac{\sqrt{\sigma_e \sigma_h}}{\sigma_e + \sigma_h}(\mu_e + \mu_h) = \sqrt{A_2}]$ extracted from the low-field MR (*blue line*) as a comparison with that calculated by the fitting results of the two-carrier model (*red line*) of thin films with different thickness of **(e)** 170 nm, **(f)** 100 nm, **(g)** 80 nm, **(h)** 50 nm.

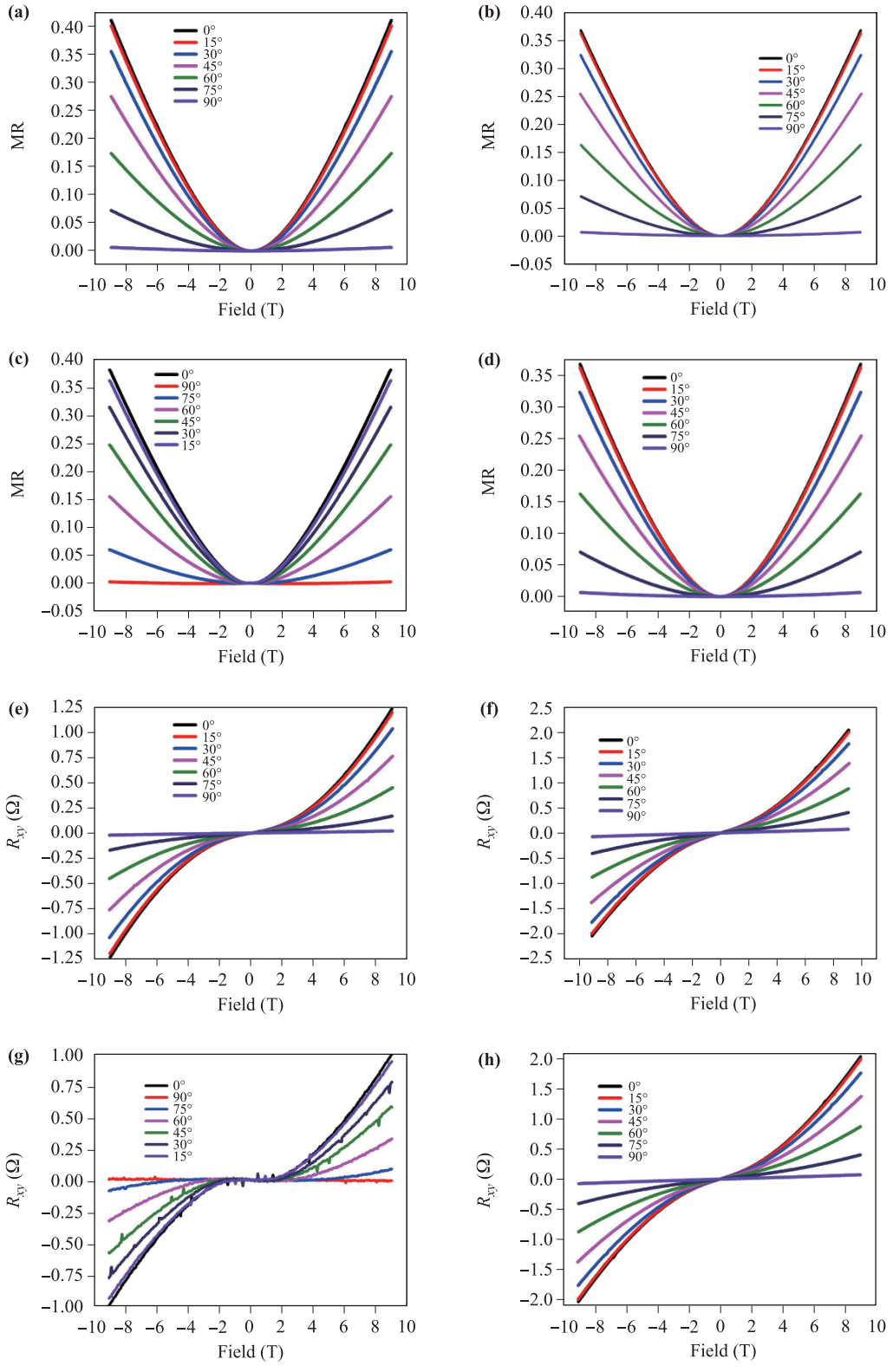

Fig. A7 MR and R_{xy} vs. external magnetic field B with different tilt angles θ of thin film with thickness of 170 nm at 2.5 K **(a, e)**, 100 nm at 2.5 K **(b, f)**, 80 nm at 2.5 K **(c, g)** and 50 nm at 3 K **(d, h)**, respectively. The angular dependence and anisotropy is clear in all these samples with different thickness.

which can be applied to the system with a constant τ over the Fermi surfaces. There should overlap with each other if there is only one kind of carriers. Nonlinear R_{xy} demonstrates that there are more than one kind of carrier. These evidence all verified the existence of two kinds of carriers. We also employed the two-carrier model as mentioned in the main text to analyze the sheet density and mobility of different carriers. On the whole, the effective mobility acquired by fitting MR at the low-field region is in accordance with the results of fitting with two-carrier model, which are obtained with $\mu = \frac{\sqrt{\sigma_e \sigma_h}}{\sigma_e + \sigma_h}(\mu_e + \mu_h)$.

Appendix D Angular dependence

Angular-dependent R_{xx} of thin film in the thickness of 80 nm in $B = 9$ T at 2.5 K is shown in Fig. A2 with tilt angle θ ranging from 0° to 360°. When the plane of the thin film is perpendicular to the filed, $\theta = 0°$ or 180°, R_{xx} acquires a wider maximum while it gets a shaper minimum when the plane is parallel to the field, $\theta = 90°$ or 270°. The difference implies the anisotropy of Fermi surfaces of $SrMnBi_2$ thin film and that the mobility of carriers along k_z direction is smaller than that along k_x, k_y direction [28]. The whole curve follows the function of $|\cos\theta|$ very well. R_{xx} and R_{xy} change along with the external field at different angles and a particular low temperature also verifies this.

References

1. K. Ziegler, Robust transport properties in graphene, *Phys. Rev. Lett.* 97(26), 266802 (2006)
2. A. K. Geim and K. S. Novoselov, The rise of graphene, *Nat. Mater.* 6, 183 (2007)
3. B. A. Bernevig, T. L. Hughes, and S. C. Zhang, Quantum spin Hall effect and topological phase transition in HgTe quantum wells, *Science* 314(5806), 1757 (2006)
4. J. Moore, Topological insulators: The next generation, *Nat. Phys.* 5(6), 378 (2009)
5. T. Liang, Q. Gibson, M. N. Ali, M. Liu, R. J. Cava, and N. P. Ong, Ultrahigh mobility and giant magnetoresistance in the Dirac semimetal Cd_3As_2, *Nat. Mater.* 14(3), 280 (2015)
6. M. Z. Hasan and C. L. Kane, Topological insulators, *Rev. Mod. Phys.* 82(4), 3045 (2010)
7. K. S. Novoselov, S. V. Morozov, T. M. G. Mohinddin, L. A. Ponomarenko, D. C. Elias, R. Yang, I. I. Barbolina, P. Blake, T. J. Booth, D. Jiang, J. Giesbers, E. W. Hill, and A. K. Geim, Electronic properties of graphene, *physica status solidi(b)*, 244(11), 4106 (2007)
8. A. Narayanan, M. D. Watson, S. F. Blake, N. Bruyant, L. Drigo, Y. L. Chen, D. Prabhakaran, B. Yan, C. Felser, T. Kong, P. C. Canfield, and A. I. Coldea, Linear magnetoresistance caused by mobility fluctuations in n-doped Cd_3As_2, *Phys. Rev. Lett.* 114(11), 117201 (2015)
9. A. A. Abrikosov, Quantum magnetoresistance, *Phys. Rev. B* 58(5), 2788 (1998)
10. D. K. S. Bertolazzi and A. Kis, Nonvolatile memory cells based on MoS_2-graphene heterostructures, *ACS Nano* 7(4), 7 (2013)
11. S. J. Han, A. V. Garcia, S. Oida, K. A. Jenkins, and W. Haensch, Graphene radio frequency receiver integrated circuit, *Nat. Commun.* 5, 3086 (2014)
12. L. Yu, Y. H. Lee, X. Ling, E. J. Santos, Y. C. Shin, Y. Lin, M. Dubey, E. Kaxiras, J. Kong, H. Wang, and T. Palacios, Graphene/MoS_2 hybrid technology for large-scale two-dimensional electronics, *Nano Lett.* 14(6), 3055 (2014)
13. J. B. He, D. M. Wang, and G. F. Chen, Giant magnetoresistance in layered manganese pnictide $CaMnBi_2$, *Appl. Phys. Lett.* 100(11), 112405 (2012)
14. Y. F. Guo, A. J. Princep, X. Zhang, P. Manuel, D. Khalyavin, I. I. Mazin, Y. G. Shi, and A. T. Boothroyd, Coupling of magnetic order to planar Bi electrons in the anisotropic Dirac metals $AMnBi_2$ (A = Sr, Ca), *Phys. Rev. B* 90, 075120 (2014)
15. M. A. Farhan, G. Lee, and J. H. Shim, $AEMnSb_2$ (AE = Sr, Ba): A new class of Dirac materials, *J. Phys.: Condens. Matter* 26(4), 042201 (2014)
16. K. Wang, L. Wang, and C. Petrovic, Large magnetothermopower effect in Dirac materials (Sr/Ca)$MnBi_2$, *Appl. Phys. Lett.* 100(11), 112111 (2012)
17. H. Masuda, H. Sakai, M. Tokunaga, Y. Yamasaki, A. Miyake, J. Shiogai, S. Nakamura, S. Awaji, A. Tsukazaki, H. Nakao, Y. Murakami, T. Arima, Y. Tokura, and S. Ishiwata, Quantum Hall effect in a bulk antiferromagnet $EuMnBi_2$ with magnetically confined 2d Dirac fermions, *Sci. Adv.* 2(1), e1501117 (2016)
18. K. F. Wang, D. Graf, H. C. Lei, S. W. Tozer, and C. Petrovic, Quantum transport of two-dimensional Dirac fermions in $SrMnBi_2$, *Phys. Rev. B* 84, 220401(R)
19. J. Park, G. Lee, F. Wolff-Fabris, Y. Y. Koh, M. J. Eom, Y. K. Kim, M. A. Farhan, Y. J. Jo, C. Kim, J. H. Shim, and J. S. Kim, Anisotropic Dirac fermions in a Bi square net of $SrMnBi_2$, *Phys. Rev. Lett.* 107(12), 126402 (2011)
20. J. Park, G. Lee, F. Wolff-Fabris, Y. Y. Koh, M. J. Eom, Y. K. Kim, M. A. Farhan, Y. J. Jo, C. Kim, J. H. Shim, and J. S. Kim, Anisotropic Dirac fermions in a Bi square net of $SrMnBi_2$, *Phys. Rev. Lett.* 107, 126402

21. A. Kobayashi, S. Katayama, Y. Suzumura, and H. Fukuyama, Massless fermions in organic conductor, *J. Phys. Soc. Jpn.* 76(3), 034711 (2007)
22. H.-H. Kuo, J.-H. Chu, S. C. Riggs, L. Yu, P. L. McMahon, K. De Greve, Y. Yamamoto, J. G. Analytis, and I. R. Fisher, Possible origin of the nonmonotonic doping dependence of the in-plane resistivity anisotropy of $Ba(Fe_{1-x}T_x)_2As_2$ (T = Co, Ni, and Cu), *Phys. Rev. B* 84, 054540
23. K. K. Huynh, Y. Tanabe, and K. Tanigaki, Both electron and hole Dirac cone states in $Ba(FeAs)_2$ confirmed by magnetoresistance, *Phys. Rev. Lett.* 106(21), 217004 (2011)
24. L. Kouwenhoven and L. Glazman, Revival of the Kondo effect, *Phys. World* 14(1), 33 (2001)
25. S. Ishiwata, Y. Shiomi, J. S. Lee, M. S. Bahramy, T. Suzuki, M. Uchida, R. Arita, Y. Taguchi, and Y. Tokura, Extremely high electron mobility in a phonon-glass semimetal, *Nat. Mater.* 12(6), 512 (2013)
26. A. Husmann, J. B. Betts, G. S. Boebinger, A. Migliori, T. F. Rosenbaum, and M. L. Saboung, Megagauss sensors, *Nature* 417, 421 (2002)
27. J. Xiong, S. K. Kushwaha, Tian Liang, J. W. Krizan, M. Hirschberger, Wudi Wang, R. J. Cava, and N. P. Ong, Evidence for the chiral anomaly in the Dirac semimetal Na_3Bi, *Science* 350(6259), 413 (2015)
28. J. Park, G. Lee, F. Wolff-Fabris, Y. Y. Koh, M. J. Eom, Y. K. Kim, M. A. Farhan, Y. J. Jo, C. Kim, J. H. Shim, and J. S. Kim, Anisotropic Dirac fermions in a Bi square net of $SrMnBi_2$, *Phys. Rev. Lett.* 107, 126402 (2011)